Revista de Metalurgia
Vol. 53, Issue 1, January–March 2017, e089
ISSN-L: 0034-8570
http://dx.doi.org/10.3989/revmetalm.089

Cleanliness distribution of high-carbon chromium bearing steel billets and growth behavior of inclusions during solidification

Chao Gu, Yan-ping Bao✉, Lu Lin

State Key Laboratory of Advanced Metallurgy, University of Science and Technology Beijing, 30 Xueyuan Road, Haidian District, Beijing 100083, P.R. China
✉Corresponding author: 15210951549@sina.cn

Submitted: 1 February 2016 Accepted: 20 February 2017 Available On-line: 27 March 2017

ABSTRACT: Variation of cleanliness and distribution of inclusions in thickness and width direction of high-carbon chromium bearing steel billets has been studied using total oxygen and nitrogen analysis and SEM/EDS, and the growth behavior of inclusions during solidification was studied with the help of solidification model. The region with relatively high total oxygen contents in the cross profile of billets is between inner arc side 3/16 and outer arc side 1/4; between left edge side 5/16 and right edge side 5/16. The formation sequence of inclusions is $MgO\text{-}Al_2O_3$ > TiN > MnS. MnS could wrap $MgO\text{-}Al_2O_3$ and reduces the damage to steel matrix caused by the latter, but generally could not effectively wrap TiN. Besides, TiN could wrap $MgO\text{-}Al_2O_3$ before MnS, which would weaken the protective capacity of MnS. Moreover, compared with $MgO\text{-}Al_2O_3$ inclusions, the sizes of TiN inclusions are generally larger. Thus the control of TiN inclusions should be strengthened. In thickness direction, the maximum size regions of TiN and MnS inclusions are inner arc side 1/3 and outer arc side 1/3; in width direction, the regions are edge side 1/3. During bearing processing, these regions and the regions with high total oxygen content should be avoided.

KEYWORDS: Billets; Distribution of inclusions; Formation sequence; Total oxygen contents

Citation / Citar como: Gu, C.; Bao, Y.P.; Lin, L. (2017) "Cleanliness distribution of high-carbon chromium bearing steel billets and growth behavior of inclusions during solidification". *Rev. Metal.* 53(1): e089. http://dx.doi.org/10.3989/revmetalm.089

RESUMEN: *Distribución y crecimiento de inclusiones en la solidificación de barras de acero para rodamientos con cromo y alto contenido de carbono*. La distribución de inclusiones en las secciones transversales y longitudinales de barras de acero para rodamientos al cromo con alto contenido de carbono se ha estudiado determinando el contenido total de nitrógeno y oxígeno y mediante SEM/EDS. El crecimiento de inclusiones durante la solidificación se estudió con la ayuda del modelo de solidificación. La zona con contenido total de oxígeno relativamente alto en la sección transversal de las barras, es entre el arco interior de 3/16 y el exterior 1/4; entre el borde izquierdo 5/16 y el derecho 5/16. La secuencia de formación de las inclusiones es $MgO\text{-}Al_2O_3$ > TiN > MnS. El MnS podría envolver a los óxidos de magnesio y aluminio ($MgO\text{-}Al_2O_3$) y reducir el daño causado al acero, pero generalmente no podría envolver al TiN. Aparte, el TiN podría envolver a los óxidos de magnesio y aluminio ($MgO\text{-}Al_2O_3$) antes que al MnS, debilitando de este modo la capacidad protectora del MnS. Además, en comparación con las inclusiones de $MgO\text{-}Al_2O_3$, las inclusiones de TiN son generalmente más grandes, por lo que es necesario controlar la formación de estas inclusiones. En la sección longitudinal, el tamaño máximo de las inclusiones de TiN y MnS son arco interno 1/3 y exterior 1/3; en la dirección del ancho, las regiones son borde 1/3. Estas regiones y las aquellas con altos contenido de oxígeno deben evitarse en el procesado de rodamientos.

PALABRAS CLAVE: Barras; Contenido total de oxígeno; Distribución de inclusiones; Secuencia de formación

ORCID ID: Chao Gu (http://orcid.org/0000-0002-0668-4859); Yan-ping Bao (http://orcid.org/0000-0002-1881-0939); Lu Lin (http://orcid.org/0000-0002-3096-4164)

1. INTRODUCTION

With the rapid development of high-speed railway technology in China, the quality of bearing steel used in high-speed railway is under severe test. The service environment is complex and the cleanliness requirements are extremely high. Under high-speed repeated load, even tiny quality problem could have large impact on the service life of bearing steel (Hua *et al.*, 2013; Mazzù *et al.*, 2015; Moghaddam *et al.*, 2015). The non-metallic inclusions failed to be removed during melting process remain in the billets of bearing steel and will not disappear in the following heat treatment. These inclusions normally become key factors that shorten the service life of bearing steel. Efforts have been made to investigate the formation mechanism and evolution of inclusions during melting process (Guo *et al.*, 2013; Ma *et al.*, 2014; Yang *et al.*, 2015; Zhang *et al.*, 2015a; Zhao *et al.*, 2015), however few studies have been carried out on the evolution of cleanliness, also the same for the distribution and size evolution of inclusions in billet. Wang *et al.* (2015) studied the cleanliness evolution in the thickness direction of IF steel billets and found that the inclusion types and cleanliness changed with positions in billets.

In present study, typical high-carbon chromium bearing steel GCr15, which is widely used in China, is set as the research object. The cleanliness evolution and the type, distribution, and size variation of inclusions were investigated. The formation sequence of all kinds of inclusions during solidification process, the inclusion size variation in the thickness-direction and width-direction of billet, the dominant area of total oxygen content, and the control direction of how to optimize inclusions were made clear, which could help guide the industrial production of bearing. Thanks to this, during bearing processing, accumulation regions of larger inclusions and high total oxygen contents in billets could be avoided, and high cleanliness part could be used. It is of great significance for improving the quality of GCr15 bearing steel.

2. EXPERIMENTAL STUDIES

The sectional dimension of the GCr15 billet used in present study is 204×189 mm, the average compositions tested by Thermo spark direct-reading spectrometer are shown in Table 1.

2.1. Analysis of total oxygen contents and nitrogen contents

Total 17 cylindrical samples (ϕ5×45 mm) were taken on the cross profile of GCr15 billet. The sketches is shown in Fig. 1a. As shown in the figure, at the center line through the width direction of billet cross profile, 9 samples were taken every other 13.75 mm respectively from inner to outer arc; 5 samples were taken every other 37.5 mm from inner to outer arc in the middle of the longitudinal centerline and the edge of billet; 3 samples were taken every other 85 mm from inner to outer arc on the edge of the billet.

The total oxygen contents and nitrogen contents of the 17 cylindrical samples were analyzed with infrared absorption method and thermal conductivity method to study the content distributions of total oxygen and nitrogen on the cross profile of GCr15 billet.

2.2. Analysis of micro-inclusions

13 metallographic specimens (No.1~13) were taken at the center line of width-direction of billet cross profile and 3 other metallographic specimens (No.14~16) were taken in the center line of thickness-direction. The sketches are shown in Fig. 1b. The specimen size of No. 5, 6, 8, and 9 was 7.5×15×15 mm and the specimen size of other 12 pieces was 15×15×15 mm. These metallographic samples were polished by SiC paper and diamond suspensions to characterize the inclusions through observations in a Scanning Electron Microscope (SEM). The chemical compositions of inclusions were analyzed by Energy Dispersive Spectrometry (EDS) combined with the SEM.

2.3. Observation of secondary dendrite arm

The metallographic specimens numbered as 1, 2, 4, and 7 (in the position of inner arc, inner arc side 1/6, inner arc side 1/3, and center of the billet respectively) were corroded with 4% Nital, and then cleaned out with absolute ethyl alcohol and blow-dried. These corroded metallographic specimens were observed through optical microscope to study the variation of secondary arm spacing (SDAS) in GCr15 billet with solidification.

3. RESULTS AND DISCUSSION

3.1. Variation of total oxygen contents and nitrogen contents

The color map of total oxygen contents in cross profile of billet is showed in Fig. 2. This color map was plotted using the griddata v4 method with MATLAB (version R2014b) based on the 17 total oxygen test results in different positions shown in Fig. 1a.

From Fig. 2, it is clear that the change rule of total oxygen contents in thickness-direction of billet is as below: the total oxygen contents in inner arc and outer arc are relatively low, and gradually

TABLE 1. Average compositions of GCr15 billet used in present study (wt%)

C	Si	Mn	P	S	Cr	Ti	Al	Cu
1.009	0.282	0.346	0.00861	0.00142	1.377	0.00168	0.0233	0.0764

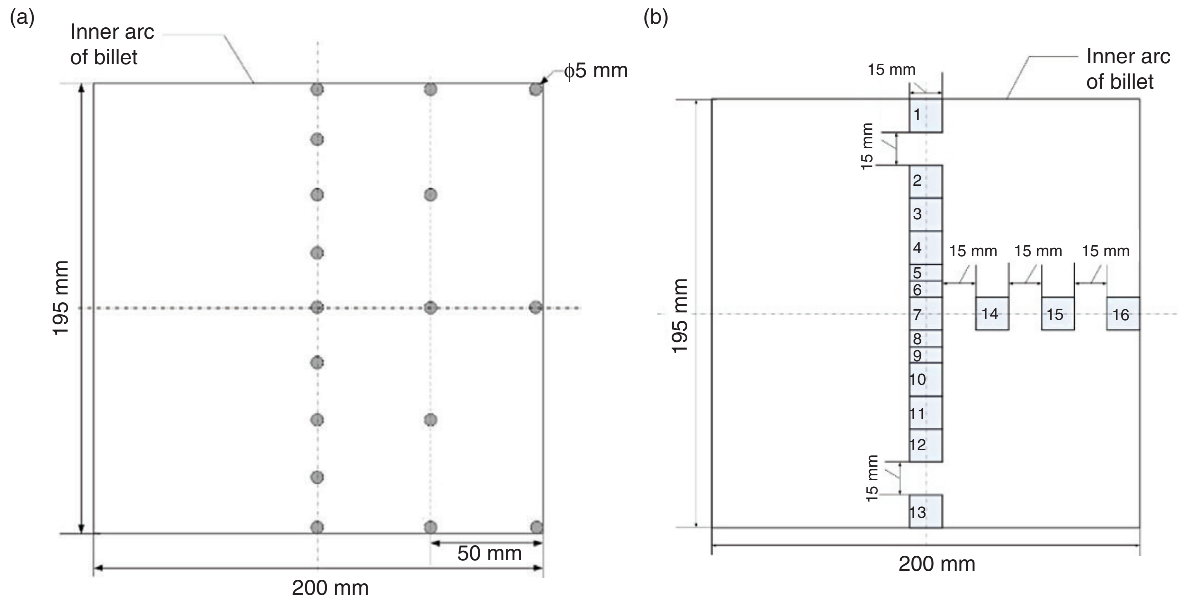

FIGURE 1. Sampling schemes: (a) cylindrical samples for total oxygen contents and nitrogen contents analysis; and (b) metallographic specimens for inclusions observation.

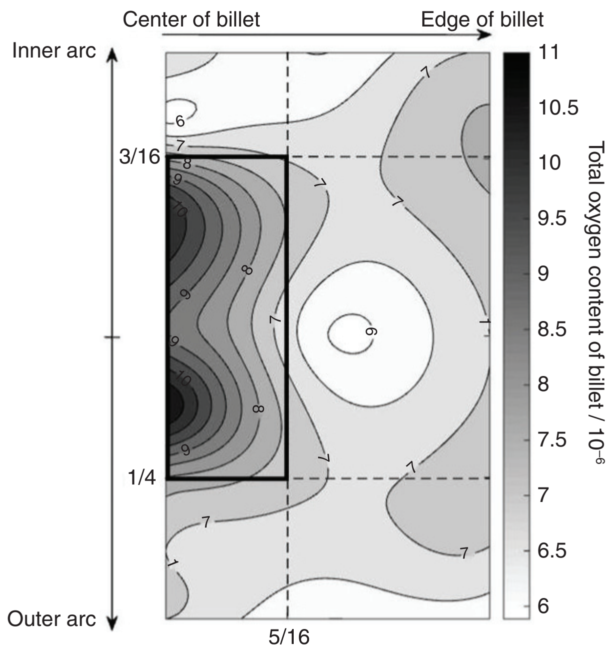

FIGURE 2. Distribution of total oxygen contents on the cross profile of GCr15 billet.

increase from inner arc side 3/16 and outer arc side 1/4. The total oxygen contents in the center of billet show a slight decline, but still higher than those in inner arc and outer arc. The change rule of total oxygen contents in width-direction of billet is that the total oxygen contents in the center are relatively high and those near the edge of billet are lower. Therefore, the region with high total oxygen content in the cross profile of GCr15 billet is shown as the solid border in Fig. 2 (from inner arc side 3/16 to outer arc side 1/4 and from left edge side 5/16 to right edge side 5/16). Generally, symmetry of cleanliness only exists in left side and right side of billet while the cleanliness of inner arc part and outer arc part of billet is different. Oxide inclusions usually form in molten steel, and tend to float during solidification. Consequently, the region with relatively high total oxygen content in the inner arc side is nearer the outer layer of billet compared to that in the outer arc side.

Nitrogen contents in the cross profile of GCr15 billet fluctuated within the range of $34{\sim}36\times10^{-6}$, which is pretty narrow, and the distribution rule is not apparent.

3.2. Variation of secondary arm spacing and cooling rate of billet

The morphologies of secondary dendrite arm in different positions of cross profile of GCr15 billet are shown in Fig. 3. When the carbon content in steel is over 0.15wt%, the relation among secondary

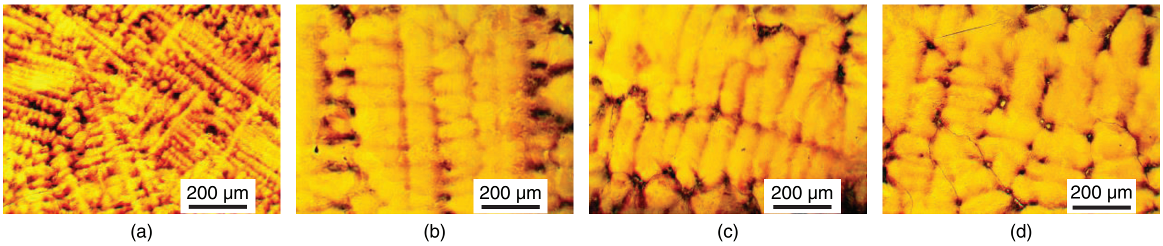

FIGURE 3. Morphologies of secondary dendrite arm on cross profile of GCr15 billet: (a) inner arc; (b) 37.5 mm from inner arc; (c) 67.5 mm from inner arc; and (d) 97.5 mm from inner arc.

TABLE 2. Cooling rates and secondary arm spacings on cross profile of GCr15 billets

Postions	Secondary arm spacing (μm)	Cool rate (°C·s^{-1})
Inner arc	36.8	8.9
37.5 mm from inner arc (inner arc side 1/6)	85.2	1.2
67.5 mm from inner arc (inner arc side 1/3)	102.0	0.8
97.5 mm from inner arc (center of the billet)	208.8	0.1

arm spacing, cooling rate, and carbon content is shown in Eq. (1) (Wolf *et al.*, 1982):

$$\lambda_2 = 104 R_c^{-0.38} \tag{1}$$

where λ_2 is secondary arm spacings (μm); R_c is cooling rate (°C/s). With the observed secondary arm spacings and carbon content in GCr15 bearing steel (1.01 wt%), the cooling rates were calculated and results are shown in Table 2.

3.3. Distribution characteristics of inclusions

Total 667 micro-inclusions were observed in different position of GCr15 bearing steel billet. There are three main types: $MgO\text{-}Al_2O_3$, MnS, and TiN. Large inclusions will do great harm to the quality of steel. However, smaller inclusions, especially when sizes are under 1 μm, usually are considered harmless, even beneficial to the quality of steel (Yang *et al.*, 2013; Zhang, 2013). Consequently, the observation of inclusions mainly aimed at those whose sizes were above 1 μm in present study.

3.3.1. Formation sequence of inclusions

Some $MgO\text{-}Al_2O_3$ inclusions observed in GCr15 bearing steel billet were partly or totally wrapped by MnS and few $MgO\text{-}Al_2O_3$ inclusions were wrapped by TiN. Few TiN inclusions were combined with MnS. The morphologies of typical inclusions are shown in Fig. 4.

The reactions related to the generation of $MgO\text{-}Al_2O_3$, MnS, and TiN inclusions are shown as Eqs. (2)~(6) (Sigworth and Elliott, 1974; Kubaschewski *et al.*, 1993; Itoh *et al.*, 1997; Fujii *et al.*, 2000; Zhang *et al.*, 2015b), among which Eq. (2) is the formation reaction of MnS inclusions, Eq. (3) is the formation reaction of TiN inclusions. Assuming the atomic ratio of MgO to Al_2O_3 in $MgO\text{-}Al_2O_3$ type inclusions is 1, the formation reaction of $MgO\text{-}Al_2O_3$, Eq. (7), can be derived from Eqs. (4)~(6).

$$[Mn]+[S]=MnS_{(s)}\ \Delta G^{\ominus}=-168822+98.87T \tag{2}$$

$$[Ti]+[N]=TiN_{(s)}\ \Delta G^{\ominus}=-291000+107.91T \tag{3}$$

$$2[Al]+3[O]=Al_2O_{3(s)}\ \Delta G^{\ominus}=-867370+222.5T \tag{4}$$

$$[Mg]+[O]=MgO_{(s)}\ \Delta G^{\ominus}=-89960-80.0T \tag{5}$$

$$Al_2O_{3(s)}+MgO_{(s)}=Al_2O_3\cdot MgO_{(s)}\quad \Delta G^{\ominus}=-20790-15.7T \tag{6}$$

$$2[Al]+[Mg]+4[O]=MgO\cdot Al_2O_{3(s)}\quad \Delta G^{\ominus}=-936540+158.2T \tag{7}$$

Assuming the activity of solid product is 1, the formula of practical solubility product Q and equilibrium solubility product K are shown as Eqs. (8)~(13). When the system is in equilibrium, Eq. (14) can be derived.

$$Q_{\mathrm{MnS}}=[Mn\%]\cdot[S\%] \tag{8}$$

$$K_{\mathrm{MnS}}=a_{[\mathrm{Mn}]}\cdot a_{[\mathrm{S}]}=1/K^{\ominus}_{\mathrm{MnS}} \tag{9}$$

$$Q_{\mathrm{TiN}}=[Ti\%]\cdot[N\%] \tag{10}$$

$$K_{\mathrm{TiN}}=a_{[\mathrm{Ti}]}\cdot a_{[\mathrm{N}]}=1/K^{\ominus}_{\mathrm{TiN}} \tag{11}$$

$$Q_{\mathrm{MgO\cdot Al_2O_3}}=[Mg\%]\cdot[Al\%]^2\cdot[O\%]^4 \tag{12}$$

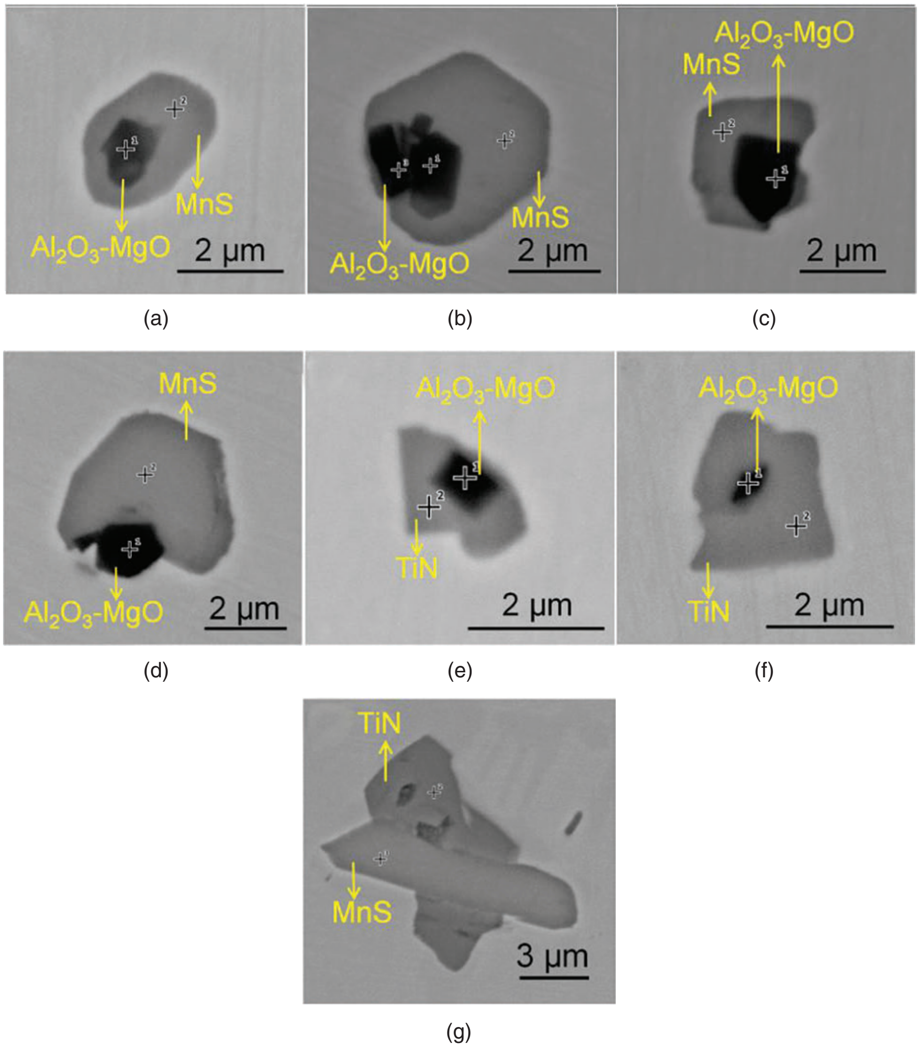

FIGURE 4. Morphologies of typical inclusions in GCr15 bearing steel billet: (a) MgO-Al_2O_3 totally wrapped by MnS; (b)–(d): MgO-Al_2O_3 partly wrapped by MnS; (e)–(f): MgO-Al_2O_3 wrapped by TiN; (g): TiN partly combined with MnS.

$$K_{Al_2O_3\cdot MgO}=a_{[Al]}^2\cdot a_{[Mg]}\cdot a_{[O]}^4=1/K_{Al_2O_3\cdot MgO}^{\ominus} \quad (13)$$

$$\Delta G^{\ominus}=-\mathrm{R}T\ln K^{\ominus} \quad (14)$$

The solidus temperature (T_L) and liquidus temperature (T_S) of high-carbon bearing steel can be calculated with Eqs. (15)~(16) (Goto *et al.*, 1995). The temperature of solidification front (T) can be calculated with Eq. (17) (Takada *et al.*, 1976):

$$T_S=1809-184.3[\%C]-40.8[\%Si]-8.6[\%Mn]$$
$$-3.4[\%Cr]-76.7[\%P]-76.7[\%S]-7.8[\%Al] \quad (15)$$

$$T_L=1809-78[\%C]-7.6[\%Si]-4.9[\%Mn]$$
$$-1.3[\%Cr]-34.4[\%P]-38[\%S]-3.6[\%Al] \quad (16)$$

$$T=T_m-\frac{T_m-T_L}{1-f_s\dfrac{T_L-T_S}{T_m-T_S}} \quad (17)$$

where T_m is the melting point of pure iron; f_s is solidification ratio.

According to Schiel equation, there is Eq. (18) (Ohnaka, 1986):

$$C_L=C_0(1-f_s)^{k_M-1} \quad (18)$$

where C_0 is solute concentration of molten steel; C_L is solute concentration in liquid phase at solidification front; k_M is distribution coefficient of solute in molten steel.

The precipitation sequence of inclusions in molten steel of GCr15 bearing steel (Fig. 5) was calculated

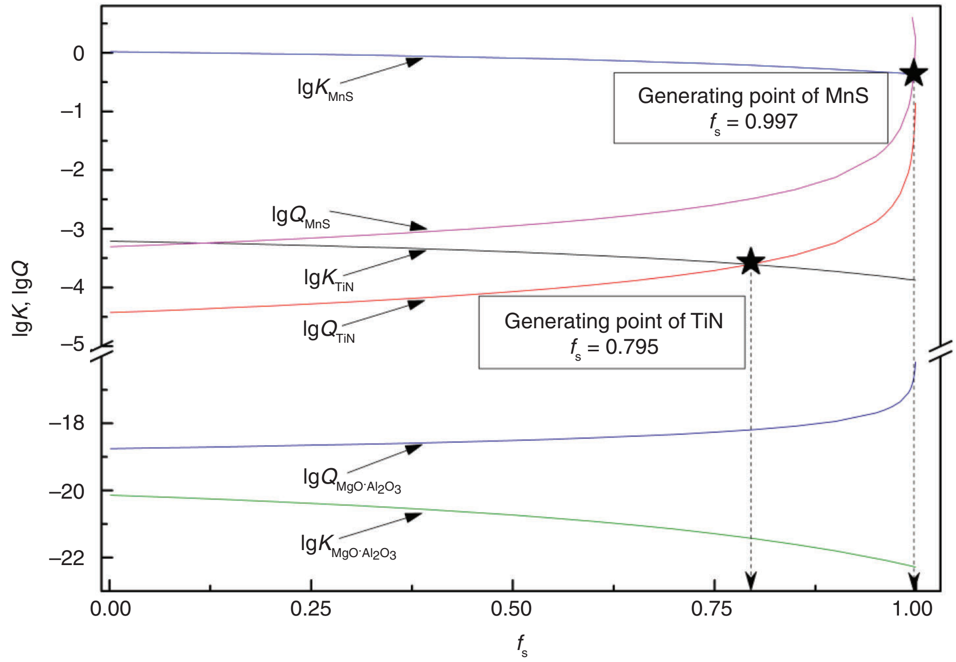

FIGURE 5. Formation sequence of inclusions in GCr15 bearing steel.

through Eqs. (2)~(14) and Eq. (17). The formation condition is met when practical solubility product Q is larger than equilibrium solubility product K. As shown in Fig. 5, it is clear that Q is always larger than K for MgO-Al_2O_3 from the beginning to the end of solidification, thus the formation of MgO-Al_2O_3 inclusions is prior to the beginning of solidification. However, TiN and MnS inclusions both generate during the solidification process of molten steel, and the solidification ratios of molten steel when they first appeared are 0.795 and 0.997 respectively.

Therefore, the formation sequence of inclusions in GCr15 bearing steel is MgO-Al_2O_3 > TiN > MnS, which corresponds with the observed wrapping status of inclusions. During solidification, the initial generating time of MgO-Al_2O_3 inclusions is far earlier than those of TiN and MnS inclusions at a certain point in billet, thus MgO-Al_2O_3 inclusions are often totally or largely wrapped by TiN and MnS. On the other hand, the initial generating times of TiN and MnS are quite close, TiN is often combined partly with MnS rather than wrapped by it. Consequently, relatively soft MnS could only protect the steel matrix from hard MgO-Al_2O_3 inclusions to a certain degree during service of bearing steel, but not for TiN inclusions, which often carry sharp edges and would do great harm to steel matrix. Moreover, due to the earlier possible generating time of TiN compared to MnS, MgO-Al_2O_3 inclusions could possibly be wrapped by TiN firstly, which could not be effectively protected by MnS. And this would increase the probability of quality problems of bearing steel.

3.3.2. Size variation of inclusions

The variations of average size of MgO-Al_2O_3, MnS, and TiN inclusions observed in the cross profile of GCr15 bearing steel billet with position are shown in Fig. 6. The average sizes are the smallest in the outer layer of billet (inner arc, out arc, and edge of billet), and increase gradually during the solidification process, reaching the maximum size in the region of inner arc side 1/3 and outer arc 1/4 in thickness direction, and edge 1/3 in width direction. The average size of TiN inclusions increases from 2.5~3.0 μm to 4.6~5.7 μm. The average size of MnS inclusions increases from 2.6~2.8 μm to 4.2~4.6 μm. After that the average sizes of these two kinds of inclusions drop slightly in the center of billet, but still larger than those in the outer layer of billet. This result is consistent with the variation tendency of inclusions in IF steel billet reported by Wang *et al.* (2015). The average size of MgO-Al_2O_3 inclusions fluctuates over the range of 1.6~2.1 μm in the whole billet and there is no obvious change in thickness direction and in width direction.

The growth of TiN and MnS inclusions in steel could be described by Eq. (19). And through integrals over Eq. (19), Eq. (20) can be derived (Ohnaka, 1986):

$$r\frac{dr}{dt}=\frac{10^6 M_S\rho_m}{M_m\rho_s}D(C_L-C_0) \tag{19}$$

$$r=10^4\sqrt{\frac{M_S\rho_m}{50M_m\rho_S}D(C_L-C_0)\tau} \tag{20}$$

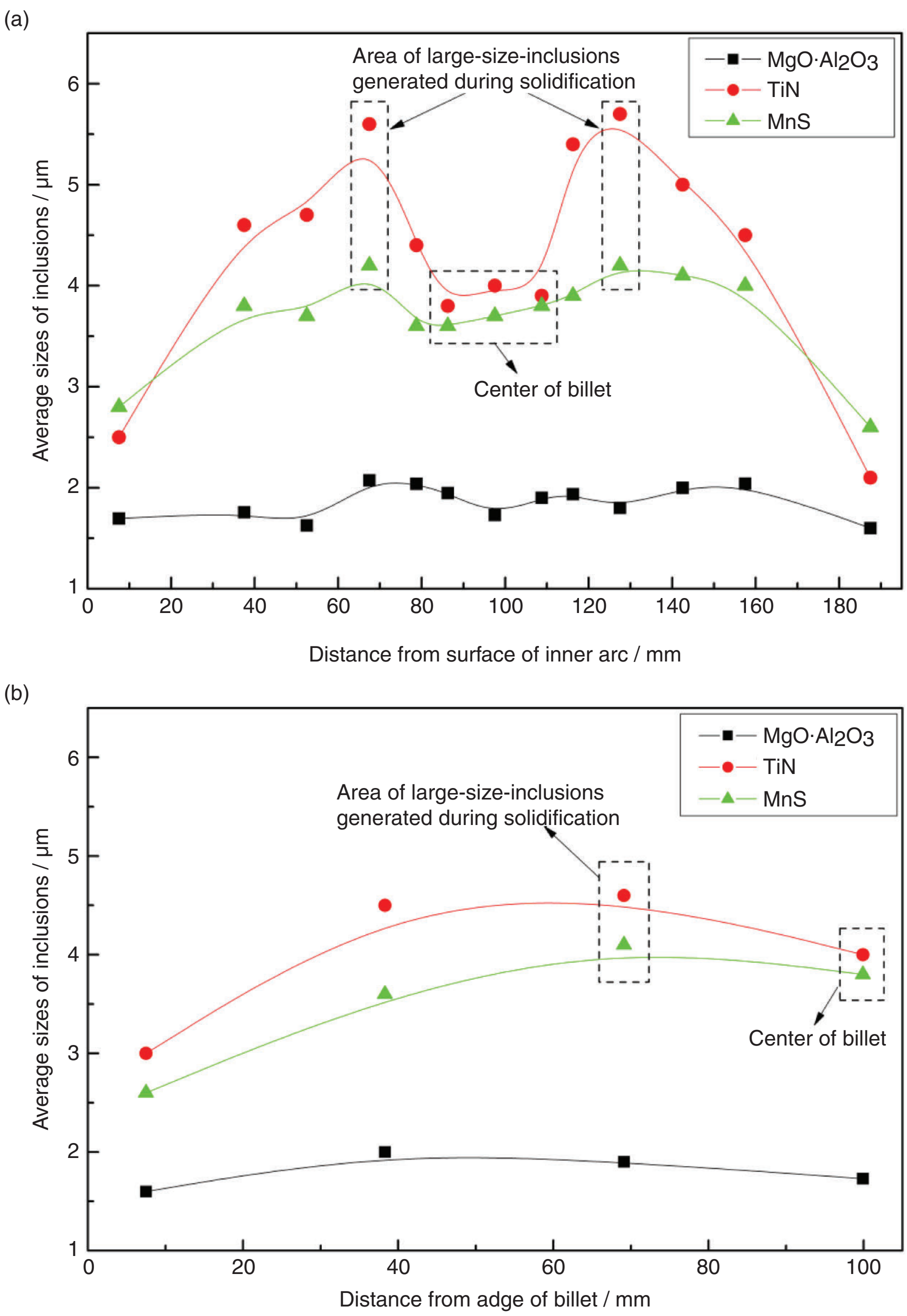

FIGURE 6. Size variation of inclusions in CGr15 bearing steel billet: (a) in thickness direction and (b) in width direction.

where r is the radius of inclusion (μm); t is solidification time (s); τ is local solidification time (s); M_m is the molar mass of Fe (0.056 kgmol^{-1}); M_S is the molar mass of inclusion (TiN: 0.062 kgmol^{-1}; MnS: 0.087 kgmol^{-1}); ρ_m is the density of Fe (7070 kg.m^{-3}); ρ_s is the density of inclusion (TiN: 5430 kg.m^{-3}; MnS: 3990 kg.m^{-3}); D is the diffusion coefficient of solute in molten steel (S: 3.9×10^{-7} cm^{2}s^{-1} (Cornelissen, 1986), N: $3.25\times10^{-3}e^{-11500/RT}$ cm^{2}s^{-1} (Wang *et al.,* 2014).The restrictive steps of the growth of TiN and MnS are the diffusion of N and S respectively. Local solidification time τ in Eq. (19) is obtained though Eq. (21):

$$\tau = \frac{T_L - T_S}{R_c} \tag{21}$$

Considering the solidification ratios f_s of molten steel are 0.795 and 0.997 respectively when TiN and MnS begin to generate, calculations of the growth of the two kinds of inclusions both begin with f_s. The calculation results are shown in Fig. 7. As shown in Fig.7, the sizes of TiN and MnS keep increasing from inner arc to the center of billet. For the same position in billet, the size of TiN is larger than MnS. This calculation result is consistent with the test result in the region from inner arc to inner arc side 1/3, but is contrary to the test result in the region from inner arc side 1/3 to the center of billet. The cause of this phenomenon is that the secondary arm spacing is smaller in the region from inner arc to inner arc side 1/3, where local solidification time is longer and thus the model error is smaller. While the secondary arm spacing is larger in the region from inner arc side 1/3 to the center of billet, where local solidification time is shorter and thus the model error is larger. Moreover, the initial size of inclusion in the kinetic model shown in Eq. (19) is simplified, which leads to a certain limitation of this model (Liu *et al.*, 2002; Yu and Li, 2015).

4. CONCLUSIONS

- The region with relatively high total oxygen content in GCr15 bearing steel billet is the center zone, more specifically from inner arc side 3/16 to outer arc side 1/4 and from left edge side 5/16 to right edge side 5/16.

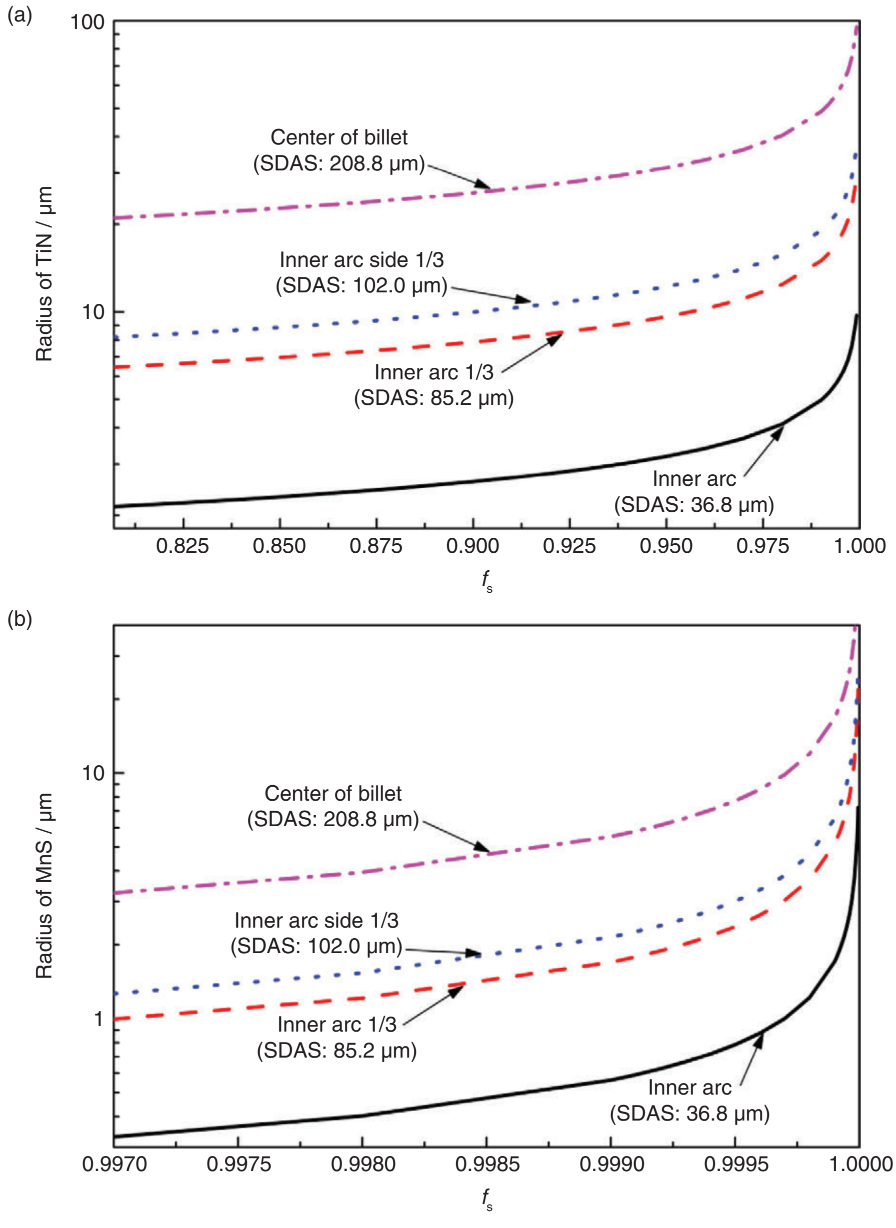

FIGURE 7. Growth tendency of inclusions in different positions of GCr15 bearing steel billet: (a) TiN; and (b) MnS.

- The main types of inclusions in GCr15 bearing steel billet are MgO-Al_2O_3, TiN, and MnS, and their formation sequence is MgO-Al_2O_3 > TiN > MnS.
- MnS inclusions could decrease the harm to steel matrix caused by MgO-Al_2O_3 inclusions, but not that effective to TiN inclusions. And TiN could possibly wrap MgO-Al_2O_3 before MnS, which would weaken the protection ability of MnS. Moreover, the sizes of TiN are generally larger than MgO-Al_2O_3. Thus the control of TiN inclusions should be strengthened while keeping MgO-Al_2O_3 inclusions in a high level considering improving quality of GCr15 bearing steel.
- In thickness direction, the maximum size regions of TiN and MnS inclusions are inner arc side 1/3 and outer arc side 1/3; in width direction, the regions are edge side 1/3. These regions as well as the regions with high total oxygen content should be avoided during machining process of bearing.

ACKNOWLEDGMENTS

This research was financially supported by State Key Laboratory of Advanced Metallurgy Foundation (N° 41614014), National Natural Science Foundation of China (N° 51574019), and Fundamental Research Funds for the Central Universities (FRF-TP-15-008A3). The authors express their appreciation to the foundation for providing financial support that guarantees the study successfully to be carried out.

REFERENCES

Cornelissen, M.C.M. (1986). Mathematical-model for solidification of multicomponent alloys. *Ironmak. Steelmak.* 13 (4), 204–212.

Fujii, K., Nagasaka, T., Hino, M. (2000). Activities of the constituents in spinel solid solution and free energies of formation of MgO, MgO·Al_2O_3. *ISIJ Int.* 40 (11), 1059–1066. http://dx.doi.org/10.2355/isijinternational.40.1059.

Goto, H., Miyazawa, K., Yamada, W., Tanaka, K. (1995). Effect of cooling rate on composition of oxides precipitated during solidification of steels. *ISIJ Int.* 35 (6), 708–714. http://dx.doi.org/10.2355/isijinternational.35.708.

Guo, J., Cheng, S.S., Cheng, Z.J. (2013). Mechanism of non-metallic inclusion formation and modification and their deformation during compact strip production (CSP) process for aluminum-killed steel. *ISIJ Int.* 53 (12), 2142–2151. http://dx.doi.org/10.2355/isijinternational.53.2142.

Hua, L. Deng, S., Han, X.H., Song Huang, S. (2013). Effect of material defects on crack initiation under rolling contact fatigue in a bearing ring. *Tribol. Int.* 66, 315–323. http://dx.doi.org/doi:10.1016/j.triboint.2013.06.008.

Itoh, H., Hino, M., Ban-ya, S. (1997). Thermodynamics on the formation of spinel nonmetallic inclusion in liquid steel. *Metall. Mater. Trans. B*. 28 (5), 953–956. http://dx.doi.org/10.1007/s11663-997-0023-5.

Kubaschewski, O., Alcock, C.B., Spenscer, P.J. (1993). *Thermochemical data. Materials Thermochemistry*. 6th Edition, Pergamon Press, pp. 257–323.

Liu, Z.Z., Wei, J., Cai, K.K. (2002). A coupled mathematical model of microsegregation and inclusion precipitation during solidification of silicon steel. *ISIJ Int.* 42 (9), 958–963. http://dx.doi.org/10.2355/isijinternational.42.958.

Ma, W.J., Bao, Y.P., Wang, M., Zhao, L.H. (2014). Effect of Mg and Ca treatment on behavior and particle size of inclusions in bearing steels. *ISIJ Int.* 54 (3), 536–542. http://dx.doi.org/10.2355/isijinternational.54.536.

Mazzù, A., Solazzi, L., Lancini, M., Petrogall, C., Ghidini, A., Faccoli, M. (2015). An experimental procedure for surface damage assessment in railway wheel and rail steels. *Wear* 342–343, 22–32. http://dx.doi.org/doi:10.1016/j.wear.2015.08.006.

Moghaddam, S.M., Sadeghi, F., Paulson, K., Weinzapfel, N., Correns, M., Bakolas, V., Dinkel, M. (2015). Effect of non-metallic inclusions on butterfly wing initiation, crack formation, and spall geometry in bearing steels. *Int. J. Fatigue.* 80, 203–215. http://dx.doi.org/doi:10.1016/j.ijfatigue.2015.05.010.

Ohnaka, I. (1986). Mathematical analysis of solute redistribution during solidification with diffusion in solid phase. *Trans. Iron Steel Inst. Jpn*. 26 (12), 1045–1051. http://dx.doi.org/10.2355/isijinternational1966.26.1045.

Sigworth, G.K., Elliott, J.F. (1974). The thermodynamics of liquid dilute iron alloys. *Met. Sci.* 8 (1), 298–310. http://dx.doi.org/10.1179/msc.1974.8.1.298.

Takada, H., Bessho, I., Ito, T. (1976). Effect of sulfur content and solidification variables on morphology and distribution of sulfide in steel ingots. *Tetsu-to-Hagane* 62 (10), 1319–1328.

Wang, Y.N., Yang, J., Bao, Y.P. (2014). Characteristics of BN precipitation and growth during solidification of BN free-machining steel. *Metall. Mater. Trans*. B. 45 (6), 2269–2278. http://dx.doi.org/10.1007/s11663-014-0146-4.

Wang, M., Bao, Y.P., Yang, Q., Zhao, L.H., Lin, L. (2015). Cleanliness evolution of interstitial free (IF) steel billets in the thickness direction. *Chinese J. Eng.* 37 (3), 307–311. http://dx.doi.org/10.13374/j.issn2095-9389.2015.03.007.

Wolf, M., Clyne, T.W., Kurz, W. (1982). Microstructure and cooling conditions of steel solidified in the continuous casting mould. *Arch Eisenhüttenwes* 53 (3), 91–92.

Yang, W., Duan, H.J., Zhang, L.F., Ren, Y. (2013). Nucleation, growth, and aggregation of alumina inclusions in steel. *JOM* 65 (9), 1173–1180. http://dx.doi.org/10.1007/s11837-013-0687-z.

Yang, L., Cheng, G.G., Li, S.J., Min Zhao, M., Gui-ping Feng, G.P. (2015). Generation mechanism of TiN inclusion for GCr15SiMn during electroslag remelting process. *ISIJ Int.* 55 (9), 1901–1905. http://dx.doi.org/10.2355/isijinternational.ISIJINT-2015-253.

Yu, H.S., Li, J.G. (2015). Size distribution of inclusions in 12% Cr stainless steel with a wide range of solidification cooling rates. International Journal of Minerals. *Int. J. Min. Met. Mater.* 22 (11), 1157–1162. http://dx.doi.org/10.1007/s12613-015-1180-1.

Zhang, L.F. (2013). Nucleation, growth, transport, and entrapment of inclusions during steel casting. *JOM* 65 (9), 1138–1144. http://dx.doi.org/10.1007/s11837-013-0688-y.

Zhang, T.S., Min, Y., Liu, C.J., Jiang, M.F. (2015a). Effect of Mg addition on the evolution of inclusions in Al–Ca deoxidized melts. *ISIJ Int.* 55 (8), 1541–1548. http://dx.doi.org/10.2355/isijinternational.ISIJINT-2014-691.

Zhang, L.F., Ren, Y., Duan, H.J., Yang, W., Sun, L.Y. (2015b). Stability diagram of Mg-Al-O system inclusions in molten steel. *Metall. Mater. Trans. B.* 46 (4), 1809-1825. http://dx.doi.org/10.1007/s11663-015-0361-7.

Zhao, D.W., Li, H.B., Bao, C.L., Yang, J. (2015). Inclusion evolution during modification of alumina inclusions by calcium in liquid steel and deformation during hot rolling process. *ISIJ Int.* 55 (10), 2115–2124. http://dx.doi.org/10.2355/isijinternational.ISIJINT-2015-064.